Int J Adv Manuf Technol (2018) 94:315–326
DOI 10.1007/s00170-017-0878-9

ORIGINAL ARTICLE

Defect classification of laser metal deposition using logistic regression and artificial neural networks for pattern recognition

Haythem Gaja[1] · **Frank Liou**[1]

Received: 5 April 2017 / Accepted: 24 July 2017 / Published online: 10 August 2017

Abstract Detecting laser metal deposition (LMD) defects is a key element of evaluating the probability of failure of the produced part. Acoustic emission (AE) is an effective technique in LMD defect detection. This work presents a systematic experimental investigation of using AE technique for detecting and classifying different defects in LMD. The defects generated during LMD simulate AE sources on deposited material while the AE sensor was mounted on the substrate to capture AE signals. An experiment was conducted to investigate the ability of AE to detect and identify defects generated during LMD using a logistic regression (LM) model and an artificial neural network (ANN). AE features, such as peak amplitude, rise time, duration, energy, and number of counts along with statistical features were extracted and analyzed. Additionally, frequency analysis using fast Fourier transformation was conducted on the AE signal. The results show that AE has considerable potential in LMD monitoring for assessing the overall deposition quality and identifying defects that can significantly reduce the strength and reliability of deposited material, and consequently, increase the risk of a component's failure.

Keywords Laser metal deposition · Deposition defects · Acoustic emission · Artificial neural network · Logistic regression · Machine learning

✉ Haythem Gaja
hmgkc7@mst.edu

[1] Department of Mechanical and Aerospace Engineering, Missouri University of Science and Technology, Rolla, MO 65409, USA

1 Introduction

Laser metal deposition (LMD) is an advanced additive manufacturing (AM) process used to build or repair metal parts layer by layer for a range of different applications. Any presence of deposition defects in the part produced causes change in the mechanical properties that might cause failure to the part. Using remedies to fix these defects will increase the machining time and costs. Monitoring the LMD process is crucial for detecting any undesired defects in the produced part and for avoiding corrective actions. Therefore, early detection is critical. Because different defect mechanisms can produce similar waveforms, the analysis and the modeling of the acoustic emission signals during the deposition process are essential, and an online detection system of any significant changes in those signals is required to detect these changes.

LMD is one type of powder-based laser deposition additive manufacturing techniques such as laser cladding [2, 3], laser direct casting [4, 5], direct metal deposition [6], directed light fabrication [7–9], laser forming [10], shape deposition manufacturing [11], laser engineered net shaping [12, 13], free-form laser consolidation [14, 15], and many others. The main process parameters of LMD are laser power, travel velocity, and powder flow rate. These parameters control the geometry accuracy and the mechanical properties of the finished part by determining the size of the molten pool, the part deformation, and the microstructure of the deposited layers. Additionally, they affect the temperature profile and cooling rate in the molten pool, as well as the thermal cycles at each location of the fabricated part [1].

The acoustic emission sensor is a piezoelectric transducer that generates an electrical charge in response to the elastic waves emitted from sources inside of a material as a result of a sudden release of energy. The AE technique is one of most powerful monitoring technologies available; it has been used

for monitoring in many manufacturing processes such as the cutting operations [16–18] and the welding process. Jolly [19] monitored the crack growth in stainless steel welds, and it was found that a maximum AE rate is directly related to the number of cracks in the weld defect zone. This work is considered to be the first significant milestone in the application of the AE technique for monitoring the welding process. A.S. Sun. Rostek [20] in 1990 used computer-aided acoustic pattern recognition to demonstrate the monitoring capabilities of acoustic signals. Duley and Mao [21] studied the laser welding process of aluminum 1100 using acoustic emission. They found that a keyhole could be identified by a specific AE frequency component, and they could then correlate the AE with laser penetration and surface condition. Grad et al. [22] in 1996 developed a monitoring method that uses different statistical parameters to assess process stability.

Bohemen [23] demonstrated that martensite formation during gas tungsten arc (GTA) welding of steel 42CrMo4 can be monitored by means of AE. It was shown that a particular relation exists between the root mean square (RMS) value of the measured AE and the volume rate of the martensite formation during GTA welding. Grad et al. [24] examined the acoustic waves generated during short-circuit gas metal arc welding process. It was found that the acoustic method could be used to assess welding process stability and to detect the severe discrepancies in arc behavior.

Yang [25] used an acoustic emission (AE) sensor to identify damage in metallic materials. Results suggested a strong correlation between AE features (i.e., RMS value of the reconstructed acoustic emission signal), surface burn, residual stress value, and hardness of steels. Diego-Vallejo [26] found that the focus position, as an important parameter in the laser material interactions, changes the dynamics and geometric profile of the machined surface as well as the statistical properties of the measured AE signal.

Wang [27] utilized acoustic emission testing to identify crack location using two acoustic emission sensors during laser cladding process. The temperature ranges of crack generation and expansion were studied using finite element analysis (FEA). The forms and extended forms of the cracks were investigated by using optical microscope and scanning electron microscope (SEM). However, the characteristic of the acoustic emission and the features of the signal were not studied, and the microscopy investigation of cracks was not linked to the location of the crack results. The experiment and analysis results show that the amount of cracks increases with the area and thickness of coating and the cooling rate increasing.

Recently, Siracusano [28] proposed a framework for the evaluation of material damages based on the Hilbert–Huang Transform, and this framework facilitates the systematic employment of both established and promising analysis criteria. The framework also provides unsupervised tools to achieve an accurate classification of the fracture type. Bianchi [29] suggested a wavelet packet decomposition within the framework of multi-resolution analysis theory should be considered for analyzing acoustic emission signals when investigating the failure of rail-wheel contact within a fatigue and wear study. The application was shown to be adequate for analyzing such signals and filtering out their noise during real-time monitoring.

However, more research is needed to develop a technique that uses AE as a reliable measure for LMD defect detection and integrity assessment. In this paper, the defect type distinguishing of LMD is investigated by modeling the AE signals. The AE technique is suitable for examining the defect sources during LMD; it contains rich defect-related information such as crack and pore formation, nucleation, and propagation. Information on defect development is difficult to obtain by only using the AE waveform in a time domain. Thus, other features such as amplitude, energy, rise time, count, and frequency are extracted to analyze qualitative defect mechanisms. The purpose of the present work is to develop reliable prediction models of defect classification that are based on AE data acquired during LMD.

This work used logistic regression and an artificial neural network to represent the relationship between the AE signal

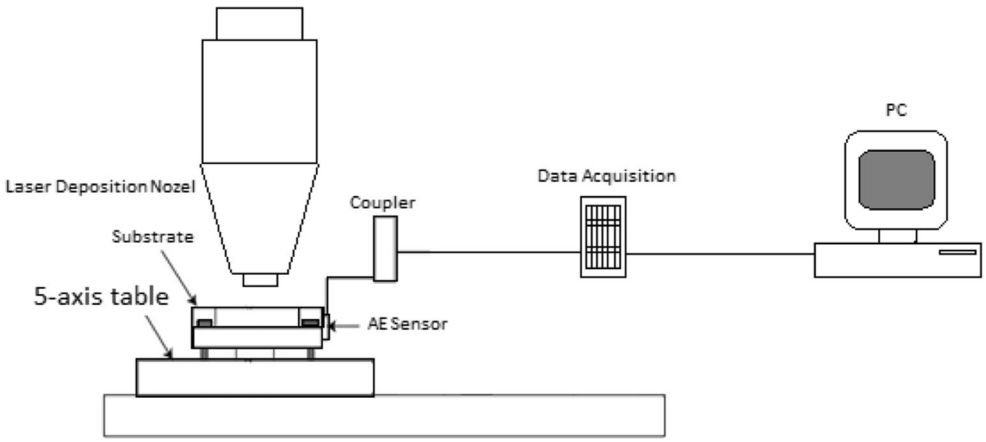

Fig. 1 Experimental setup shows the LMD system and AE data acquisition system

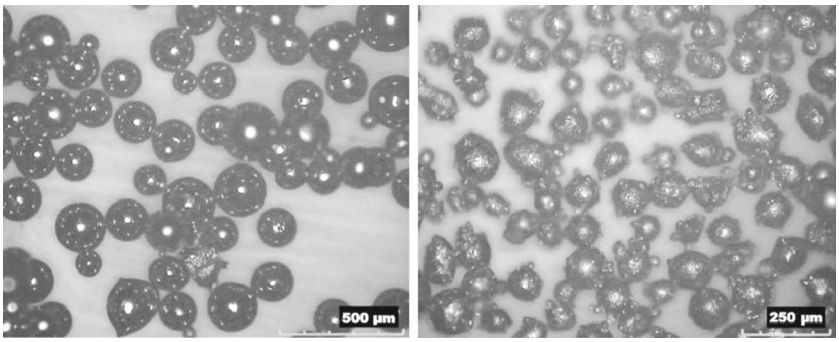

(a) Ti-6Al-4V Metal Powder (b) H13 Metal Powder

Fig. 2 **a**, **b** Optical image of the metal powders used in deposition process

and the defect types in LMD processes, and then the results of the two models were compared with the results of clustering analysis. The AE event features were fed into the two models to measure operation quality during LMD. After the models had been trained, the inference system classified the AE events in real time from the experimental sensor signal. The results of the monitoring algorithm can warn the operator to take corrective actions in order to reach the optimum quality of the produced part.

2 Experiments and data collection

Figure 1 shows a schematic diagram of the experimental set-up. The YAG laser was attached to a 5-Axis vertical computer numerical control machine that is used for post-process machining after LMD. The data acquisition system consists of acoustic emission sensor, coupler, and data acquisition oscilloscope. The used AE system (Kistler 8152B111) has a relatively superior signal-to-noise ratio and sensitivity at the ultra-precision scale. The noise level is much smaller than the signals of interest; also, a frequency filtering was used which allows the passing of only those signals falling within a selected bandwidth.

The acoustic emission sensor is made up of the sensor housing, a piezoelectric sensing element, and a built-in impedance converter. The sensing element, made of piezoelectric ceramic, is mounted on a thin steel diaphragm. Its construction determines the sensitivity and frequency response of the sensor. It is acoustically isolated from the housing by design and therefore well protected against external noise. The acoustic emission sensor is highly sensitive to surface and longitudinal waves over a broad frequency range.

The AE-Piezotron coupler comprises plug-in modules that amplify and filter the raw signal. The main function of the coupler is to supply power to the sensor and process the emission signal. The gain factor, low- and high-pass filters, and integration time constant are included in one electronic board, allowing the best possible adaptation to a specific monitoring function. The coupler provided 0–5 V voltage signals proportional to the detected defect and eliminated any need for further signal processing. Figure 3 shows the coupler assembly diagram.

Picoscope 2205A works as a dual-channel oscilloscope to capture the AE signal and stream it to a computer for further analysis. The oscilloscope measures the change in the acoustic emission signal over time, and helps in displaying the signal as a waveform in a graph. The raw signals were first fed through

Table 1 The composition and thermal properties of titanium and tool steel metallic powders (mass %)

	Ti-6Al-4V	H13
Iron, Fe	< 0.25	Balance
Chromium, Cr	–	4.75–5.5
Molybdenum, Mo	–	1.1–1.75
Silicon, Si	–	0.80–1.20
Vanadium, V	3.50 to 4.50	0.80–1.20
Carbon, C	< 0.08	0.32–0.45
Nickel, Ni	–	0.3
Manganese, Mn	–	0.20–0.50
Titanium, Ti	Balance	–
Aluminum, Al	5.50 to 6.50	–
Thermal expansion ($°K^{-1}$)	11 × 10 − 6 – 15 × 10 − 6	13 × 10 − 6 – 16 × 10 − 6
Thermal conductivity (W/mK)	8	28.6

Table 2 Time domain and frequency domain AE signal features

Feature	Definition
Peak amplitude	It is the greatest measured voltage in an AE event.
Kurtosis	It is a measure of whether the data of an AE event are peaked or flat compared to a normal distribution. $Kurtosis = \frac{\sum_{i=1}^{N}(x_i-\bar{x})^2/N}{\sigma^4} - 3$ (1) where N is the number of samples (x_i) in an AE signal, σ is the standard deviation, and $\bar{x}$ is the mean.
Energy	Since the domain of the AE event signal is discrete, the energy of the signal is given by: $Energy = \sum_{i=1}^{N}(x_i)^2$ (2)
Number of counts	It is the number of pulses emitted by the AE event.
Duration	It is the time difference between the first and last threshold crossings.
Rise time	It is the time interval between the first threshold crossing and the AE event peak.
Peak amplitude frequency	It is a characterization of the magnitude and frequency of an AE event using fast Fourier transform

the data acquisition system and then processed and recorded using Matlab software.

A powder feeder system was used to deliver the atomized powder to the melt pool using argon gas (which is also used as a shielding gas), and it flowed through channels in the nozzle of laser deposition head to reduce the oxidation of the deposit. During the laser metal deposition process, porosities and cracks can be formed as the result of a lack of fusion, shield gas trapping, and the difference in thermal coefficients of the deposited material and the substrate. The AE signal was recorded during a laser deposition process in an oxidized environment and with contaminated powder in order to induce pores and cracks as a result of thermal coefficient difference. The material of the substrate was tool steel. Cracks and porosities were simulated primarily by mixing Ti-6Al-4V powder with H13 tool steel powder. The two powder particles as illustrated in Fig. 2 are non-uniform in shape and size and may contain internal voids that can cause deposition defects when mixed. Table 1 displays the chemical composition and the thermal properties of both powders.

Different defect mechanisms can produce similar waveforms and amplitudes; it is not sufficient to use a particular feature to represent the events. Therefore, seven AE signal features (Table 2) were employed in the signal analysis to overcome this problem. Representing the AE signal with enough features is critical in order to collect as much information as possible about the emitting source, especially when there is little literature regarding the use of AE techniques for motoring LMD process that can be utilized as a reference during AE feature selection. The AE signal can be represented in the frequency domain by using fast Fourier transform (FFT) or in the time domain by using peak amplitude, kurtosis, energy, number of counts, duration, and rise time. Figure 3 shows some of the time-dependent features.

Among all of the features, the signal amplitude alone was measured in real time by the data acquisition system. Once the

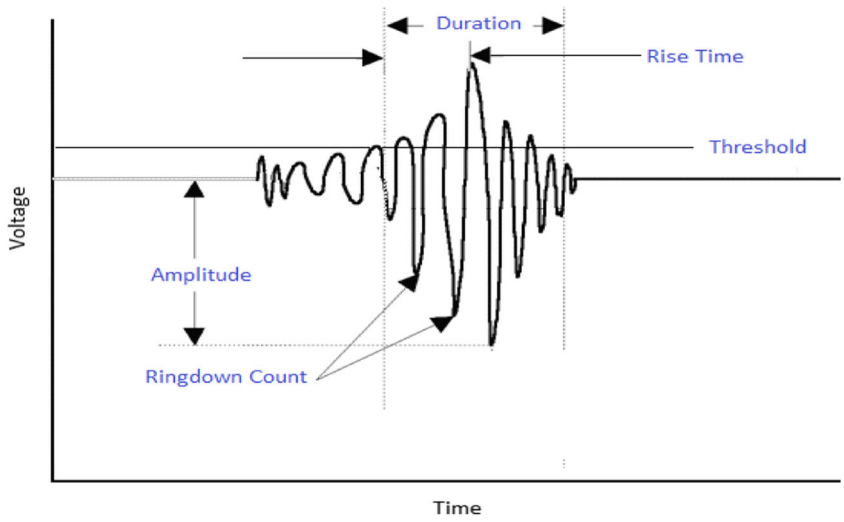

Fig. 3 Time-dependent AE event features

Table 3 Laser metal deposition process parameters

Parameter	Value
Laser power	1000 W
Powder feed rate	10 g/min
Table velocity	300 mm/min
Layer thickness	About 0.5 mm
Layer width	About 2.5 mm

AE signal is recorded, the other features were calculated from the waveforms at the end of the deposited layer because they are particularly dependent on the amplitude and threshold. In this work, all of these features were used in a multi-logistic regression statistical analysis and ANN analysis. No AE noise associated with the operation of the laser system or the CNC system was observed. Also, it was found in this study that the noise level is much smaller than the signals of interest. Additionally, a frequency filtering was used, which allowed

Table 4 Standardized AE signal features and the clustering results

Event number	Rise time	Peak amplitude	Duration	Kurtosis	Number of counts	Energy	Frequency	Defect
1	− 0.8632828	− 0.7341107	− 0.68626	− 1.44472	− 0.75435274	− 0.42589	− 1.27045	Pore
2	− 0.1261721	− 0.6508765	− 0.60598	− 1.25783	− 0.6648721	− 0.42121	− 0.28512	Pore
3	− 0.6931803	− 0.6231318	− 0.62959	−0.34811	− 0.6786384	− 0.42337	− 0.16714	Pore
4	− 0.0694712	− 0.5398975	− 0.51153	− 0.52405	− 0.5478591	− 0.41726	− 0.57824	Pore
5	− 0.2584740	− 0.4844081	− 0.55876	0.728254	− 0.5960409	− 0.4176	1.576003	Pore
6	− 0.2962745	− 0.5121528	− 0.28959	− 0.16773	− .2174693	− 0.41689	0.226959	Pore
7	− 0.5797787	− 0.5676423	− 0.53514	0.00428	− 0.5547422	− 0.42265	0.843153	Pore
8	2.803370	2.0958524	2.3407	− 1.1222	2.2535706	2.41352	0.053381	Crack
9	− 0.1072718	− 0.6786212	− 0.53987	− 0.14773	−0.5409760	− 0.42517	1.349834	Pore
10	− 0.5608784	− 0.7063660	− 0.64376	− 1.04886	− 0.6924046	− 0.42553	− 0.08978	Pore
11	− 0.3151748	0.3201892	− 0.02042	0.449555	− 0.0109757	− 0.31195	1.354937	Pore
12	− 0.3340751	− 0.4844081	− 0.68626	1.881232	− 0.7612358	− 0.42228	− 0.71316	Pore
13	2.1796615	2.0958524	1.953476	− 0.93525	1.9231809	1.795566	− 0.14501	Crack
14	− 0.1828729	− 0.5121528	− 0.29903	0.510621	− 0.2381187	− 0.41256	0.799576	Pore
15	− 0.5041776	− 0.3734291	− 0.33681	0.103122	− 0.3138330	− 0.40788	− 0.4526	Pore
16	1.8583568	2.0958524	1.967643	− 1.38266	1.7029210	2.668412	− 0.04808	Crack
17	− 0.1639726	− 0.6231318	− 0.23292	0.998504	− 0.1142225	− 0.42121	1.881284	Pore
18	0.0628306	0.9860629	0.267636	2.358211	0.3882451	− 0.26322	0.568001	Pore
19	− 0.8632828	− 0.6786212	− 0.74765	0.445735	− 0.8438333	− 0.42517	− 0.77585	Pore
20	− 0.7309809	− 0.734110	− 0.7382	− 0.56879	− 0.8300670	− 0.42589	− 0.82462	Pore
21	− 0.5986790	0.1259761	− 0.17625	0.437646	− 0.1555213	− 0.35378	− 0.48302	Pore
22	− 0.1828729	0.1814655	0.02208	0.054488	0.0785047	− 0.33756	− 0.34344	Pore
23	− 0.5797787	− 0.4566633	− 0.1007	1.929897	− 0.0109757	− 0.38877	0.603812	Pore
24	− 0.5608784	− 0.234705	− 0.28487	− 0.16722	− 0.2587681	− 0.39165	1.376322	Pore
25	− 0.0316707	0.1814655	− 0.09598	1.216332	− 0.0316251	− 0.36316	− 0.00579	Pore
26	− 0.4852773	− 0.6231318	− 0.28487	− 0.57514	− 0.1761706	− 0.42337	− 0.00107	Pore
27	− 0.2017732	− 0.4566633	− 0.41237	1.534873	− 0.3620149	− 0.4212	− 2.1943	Pore
28	− 0.4852773	− 0.7063660	− 0.51626	− 0.96409	− 0.5203266	− 0.42445	− 2.15717	Pore
29	0.0817309	− 0.6786212	− 0.42653	− 1.13012	− 0.3757811	− 0.42517	1.515988	Pore
30	0.8755425	1.9293840	0.65486	1.466014	0.8218817	0.066326	− 0.03145	Pore
31	2.7277695	2.0958524	2.760979	− 1.11484	2.8042202	2.811349	− 2.23613	Crack
32	− 0.6931803	− 0.734110	− 0.69098	0.127625	− 0.7612358	− 0.42589	0.776849	Pore
33	− 0.6931803	− 0.7063660	− 0.72403	0.144849	− 0.8094177	− 0.42553	0.102579	Pore
34	− 0.5608784	− 0.4566633	− 0.23764	− 0.33667	− 0.1899369	− 0.40212	0.40919	Pore
35	2.066259	2.0958524	2.765701	− 1.07521	2.7835709	2.630087	− 0.15449	Crack
36	− 0.8632828	− 0.6786212	− 0.67209	− 0.25692	− 0.7337033	− 0.42517	0.082367	Pore
37	− 0.0694712	0.4311682	− 0.04875	0.176898	− 0.0109757	− 0.2917	− 0.56332	Pore

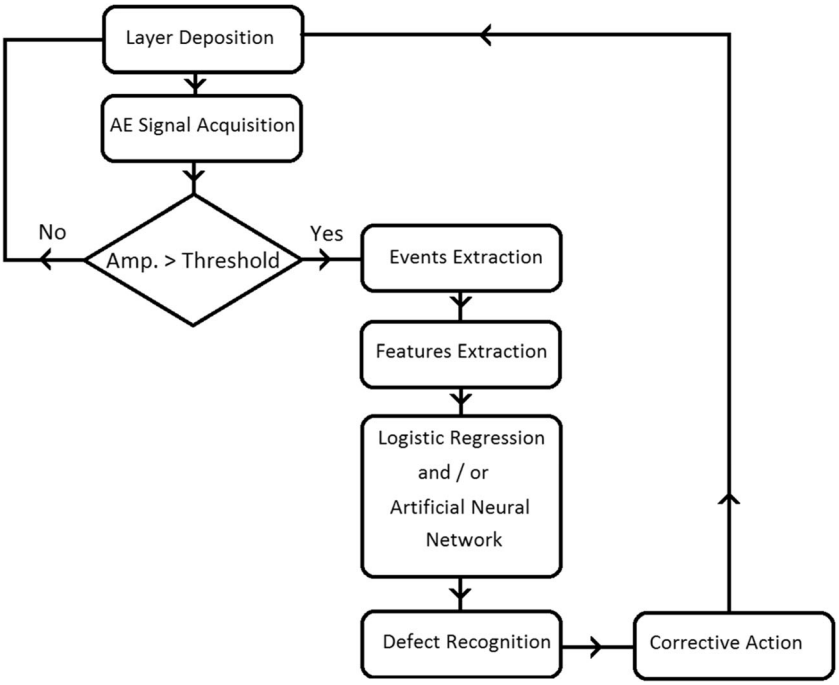

Fig. 4 Step-by-step operations used to perform the acoustic emission analyses

only those signals falling within a selected bandwidth (100 to 900 kHz) to pass through the filter.

Two depositions were performed with standard parameters for depositing titanium powder, as shown in Table 3. The first deposit was 15 mm in length and the second deposit was 5 mm in length. The first AE signal was used to group the AE events into homogeneous subgroups (clusters), and the experiment conditions, data collection, and results were discussed in detail in a previous study by the authors [30]. In this pervious study, the results were used to construct the LR and the ANN models.

Table 4 shows the AE event features and results of the signal analysis. The number of pores in the first signal was 32, while the number of cracks was found to be only 5. This data was used to create LR and ANN models. To validate how well the two models fit the data, a second AE signal was acquired under the same experimental conditions. The second set of the AE signal was used in this study to estimate the probability of a binary response crack or pore (0 or 1) based on the features of the AE events. The outcomes of the two models were compared and verified with the second AE signal.

Figure 4 illustrates the main steps in the developed procedure that was used to analyze the AE data. The AE sensor was attached to a substrate to transform the energy released by the laser deposition into an acoustic emission signal. The formation of porosities and cracks generates an acoustic emission signal, which is an elastic wave that travels from the source toward a sensor, moving through the substrate until it arrives at the acoustic emission sensor. In response, the sensor produces an electrical signal, which is passed to electronic equipment for further processing and defect detection. Since the LMD is an additive process and it deposits metals layer by layer, the AE signal was recorded for each layer and was

Table 5 Results of the regression analysis

Term	Coefficients	Standard error	*P* value
Intercept	− 12.2018419	0.0805	< 0.001
x_1	2.37719998	0.2926	< 0.001
x_2	− 4.78228419	0.2341	< 0.001
x_3	46.23988958	3.112	< 0.001
x_4	0.116482205	0.09162	0. 06
x_5	− 34.48089538	2.429	< 0.001
x_6	4.919644537	0.8852	< 0.001
x_7	− 0.06002589	0.07432	0. 217

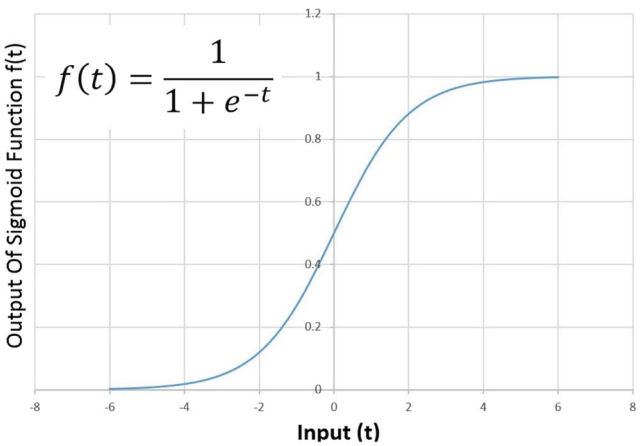

Fig. 5 Sigmoid activation function

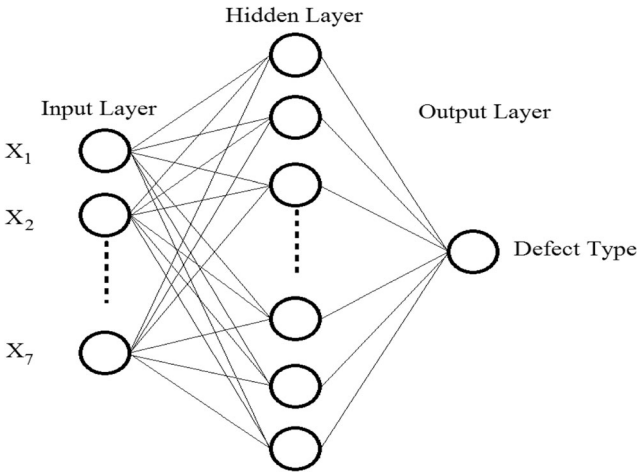

Fig. 6 Neural network architecture

analyzed in order to extract any useful information from the AE events.

3 Results and discussion

3.1 Logistic regression-based modeling

In a logistic regression, the dependent variable is binary, meaning that it can take only two values of "0" and "1," where 0 represents defect type I and 1 represents defect type II. Each of these results represents the outcomes of crack or pore, respectively. Cox [31] developed the logistic regression in 1958. The LR model is used to estimate the probability of a binary response (defect type) based on seven variables (AE event features).

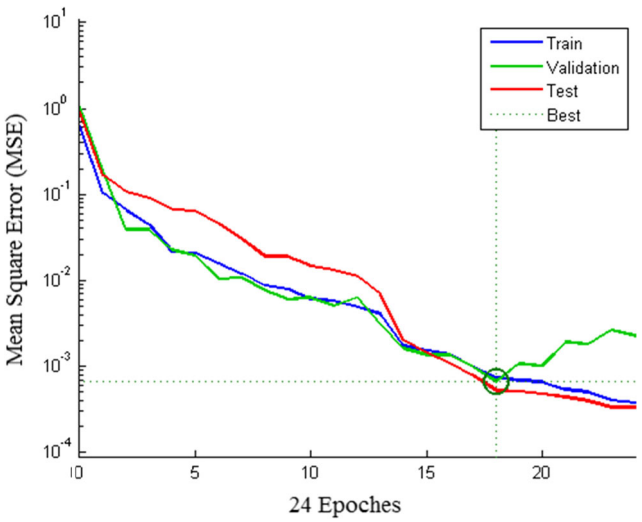

Fig. 7 Neural network performance

Logistic regression is used to model the probability of defect classification into a type I or type II defect. Let y^* indicate the classification of the ith AE event such that $y^* = 1$ if the AE event is classified as pore and $y_i^* = 0$ if the AE event is classified as crack:

$$y^* = ln\left(\frac{p}{1-p}\right) = \beta_0 + \sum_{i=1}^{n} \beta_i x_i \quad (1)$$

where β_0 is the intercept and β_i is the regression coefficient.

Table 6 Results of the logistic regression and neural network analysis

Event number	y^*	LR probability	ANN	Defect
1	2.18E + 01	1	1	1
2	2.23E + 01	1	1	1
3	2.25E + 01	1	1	1
4	2.25E + 01	1	1	1
5	2.33E + 01	1	1	1
6	2.38E + 01	1	1	1
7	2.29E + 01	1	1	1
8	− 3.40E + 01	1.66E − 15	3.42E − 07	0
9	2.36E + 01	1	1	1
10	2.25E + 01	1	1	1
11	2.16E + 01	1	1	1
12	2.32E + 01	1	1	1
13	− 1.92E + 01	4.44E − 09	2.16E − 06	0
14	2.34E + 01	1	1	1
15	2.29E + 01	1	1	1
16	− 4.00E + 01	4.18E − 18	1.17E − 06	0
17	2.42E + 01	1	1	1
18	2.61E + 01	1	1	1
19	2.16E + 01	1	1	1
20	2.15E + 01	1	1	1
21	2.31E + 01	1	1	1
22	2.24E + 01	1	1	1
23	2.12E + 01	1	1	1
24	2.32E + 01	1	1	1
25	2.48E + 01	1	1	1
26	2.44E + 01	1	1	1
27	2.47E + 01	1	1	1
28	2.24E + 01	1	1	1
29	2.45E + 01	1	1	1
30	2.60E + 01	1	0.999998	1
31	− 3.97E + 01	6E − 18	1.96E − 07	0
32	2.18E + 01	1	1	1
33	2.18E + 01	1	1	1
34	2.20E + 01	1	1	1
35	− 3.92E + 01	9.74E − 18	3.90E − 07	0
36	2.21E + 01	1	1	1
37	2.39E + 01	1	1	1

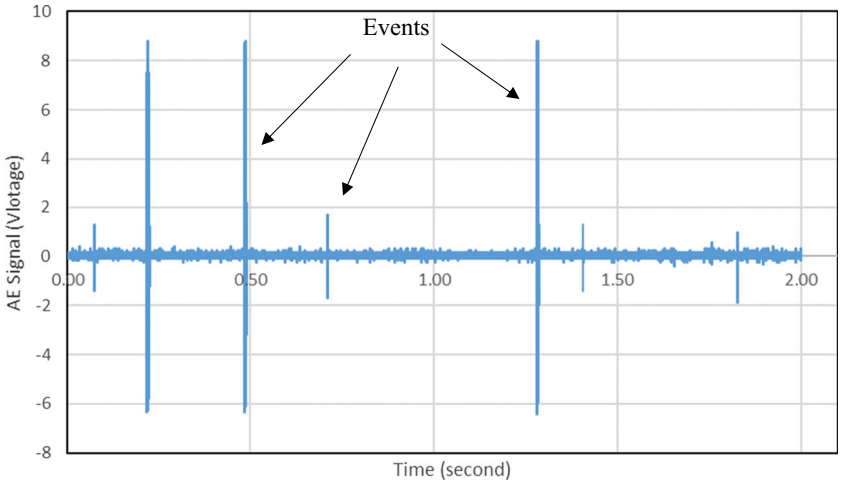

Fig. 8 AE raw signal acquired during LMD process

Therefore, the probability (p) of the porosity defect being formed is:

$$p = \left(\frac{e^{y^*}}{1 + e^{y^*}}\right). \tag{2}$$

In Table 5, x_1, x_2, x_3, x_4, x_5, x_6, and x_7 represent rise time, peak amplitude, duration, kurtosis, number of counts, energy, and frequency, respectively. By considering all terms, the LR model for defect formation is:

$$y^* = ln\left(\frac{p}{1-p}\right) = -12.2 + 2.37\,x_1 - 4.78x_2 + 46.23\,x_3 + 0.11\,x_4 - 34.48\,x_5 + 4.91x_6 - 0.06\,x_7 \tag{3}$$

3.2 Artificial neural network-based modeling

An ANN is a statistical machine-learning tool established on the idea of how neurons in a human brain work. The neural network consists of layers and nodes, called neurons, and the number of layers and neurons depends on the difficultly of the problem being modeled. The input and output layers have neurons equal to the number of the inputs and the outputs, respectively. The neurons are connected by synapses, which take a value from an input neuron, multiply it by a specific weight, and output the results. The neurons have a more complicated purpose: they add together all outputs from all synapses and apply an activation function.

A sigmoid function was used for activation. This kind of function was selected because it is one of the common types of transformation functions and because it provides a method of establishing complex, non-linear relationships between the input and output data sets, as shown in Fig. 5. A sigmoid function was used to map the output of the hidden layer to the range of values of (0, 1).

Any ANN has at least three layers: an input layer, a hidden layer, and an output layer. If X is the input data vector (which in this work is a one by seven vector as shown in Fig. 6), $W(1)$ is the weight matrix (which is a seven by N matrix, where N is the number of neurons in the hidden layer), and $Z(2)$ is the transfer function of the second layer:

$$Z^{(2)} = X \times W^{(1)} \tag{4}$$

By applying the transfer function to each element in $Z^{(2)}$, $a^{(2)}$, the activation function of the second layer, can be obtained by:

$$a^{(2)} = f\left(Z^{(2)}\right) \tag{5}$$

where $a^{(2)}$ has the same size as $Z^{(2)}$. By multiplying weight matrix of the second layer $W(2)$ (which is an N by one matrix), there is only one output in our ANN which is defect type:

$$Z^{(3)} = a^{(2)} \times W^{(2)} \tag{6}$$

where $Z^{(3)}$ is the transfer function of the third layer. Finally, the activation function is applied to $Z^{(3)}$ to obtain the estimate for defect type y':

$$y' = f\left(Z^{(3)}\right) \tag{7}$$

Table 7 Verification results of the logistic regression analysis and neural network

Event number	Clustering analysis	LR probability	ANN
1	Porosity	Porosity	Porosity
2	Crack	Crack	Crack
3	Crack	Crack	Crack
4	Porosity	Porosity	Porosity
5	Crack	Crack	Crack
6	Porosity	Porosity	Porosity
7	Porosity	Porosity	Porosity

Without training, the network's estimation error will be very large, as training is the process of updating the weight matrix in order to minimize the cost function J:

$$J = \sum \frac{1}{2}\left(y - y'\right)^2 \tag{8}$$

One of the training algorithms that can be used to train the ANN is a supervised learning algorithm called a backpropagation algorithm. This algorithm adjusts the learning rate and momentum coefficient and keeps them between 0 and 1. Equation 8 can be written as:

$$J = \sum \frac{1}{2}\left(y - f\left(f\left(XW^{(1)}\right)W^{(2)}\right)\right)^2 \tag{9}$$

In order to save time and reduce calculations, the gradient descent method is used to guarantee that the search for J is in the correct direction and stop the search when the smallest J is reached (i.e., when the cost function stops decreasing). These tasks are accomplished by taking the partial derivative of J

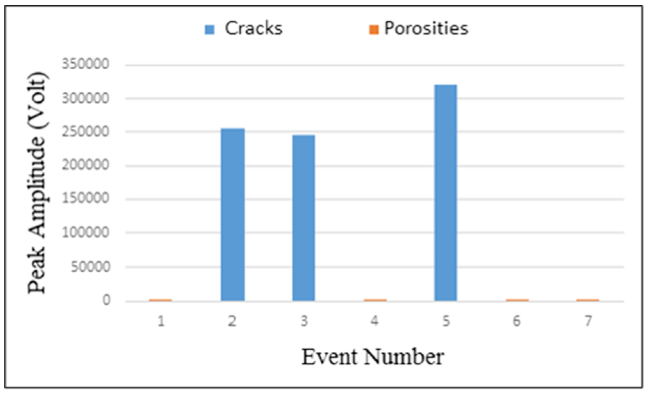

(a) Porosities produce less energy

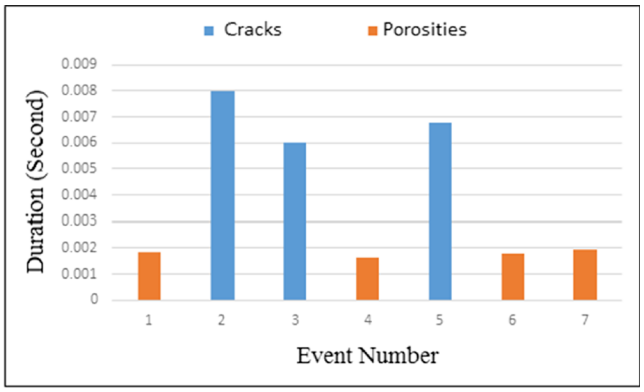

(b) Porosities have shorter duration

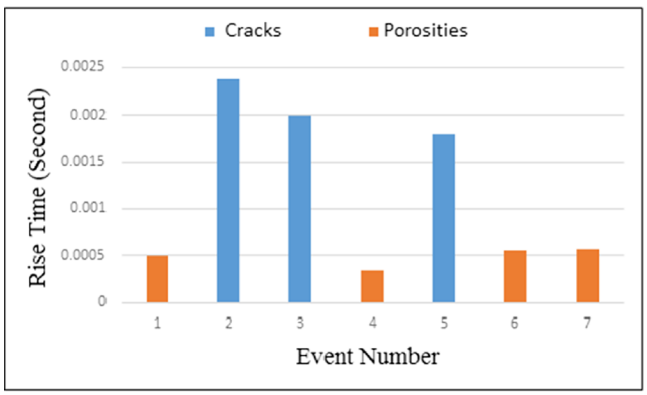

(c) Porosities in have slower rise time

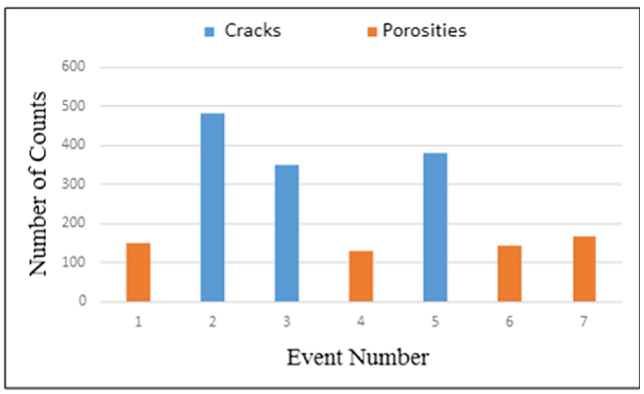

(d) Porosities have less number of counts

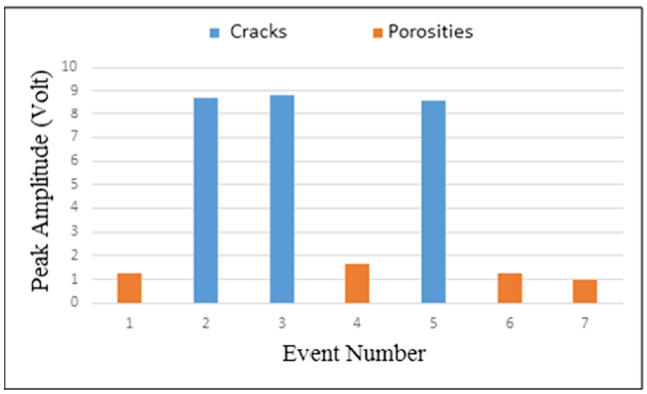

(e) Porosities have lower amplitude

Fig. 9 **a**–**e** Comparing the signal features between crack and porosities

with respect to W $\left(\frac{\partial J}{\partial W}\right)$ so that $\frac{\partial J}{\partial W}$ is positive (the cost function is increasing) and vice versa. This method is useful, especially for multi-dimensional problems. Gradient descent can be performed either after using all training data (batch gradient descent) or after each input–output pair is identified (sequential gradient descent).

The neural network was trained with 25 data points (AE signal features) to estimate the weights (included biases) of candidate designs, and six data points were used to both estimate the non-training performance error of candidate designs and stop the training once the non-training validation error estimate stopped decreasing. Also, six data points were used as testing data to obtain an unbiased estimate of the predicted error of unseen non-training data. Training, validation, and testing data were randomly chosen from different cutting conditions from the data set that consisted of 37 data points (AE signal features).

Figure 7 illustrates the mean squared error versus iteration (epochs) number while using the Bayesian regularization training algorithm. Twenty-five neurons were used within the hidden layer in this work. The network was trained for 30 iterations, at which time the performance was changed dramatically, and the best performance was 0.000661 at epoch 18.

The defects are denoted in Table 6 as a binary variable (0 or 1), where 1 represents pores, and 0 represents cracks. The mean squared error (MSE) for the LR model was 1.72973, and the error for the ANN model was 1.702703, where the ideal value of MSE is zero. The MSE defines the average of the squares of residuals, which are found when the values predicted by LR and ANN deviate from the actual values of data. In this study, the performance of the ANN model was slightly better than the LR model. Because there is an insignificant difference in the performance of the two models, they will both be used to estimate the type of defect.

3.3 Model verification (defect classification)

Figure 8 shows an AE signal acquired during the LMD process in the presence of defects. The spikes in the signal are called events, and these have features that are different from the rest of the AE signals. The AE event is counted when the amplitude of the signal is higher than a preset threshold and is preceded and followed by a signal with amplitude lower than the threshold for a specified period.

Table 7 shows the outcomes of logistic regression and neural network analysis compared to clustering analysis. Both models succeed at predicting the type of defect, and the AE signal contained three cracks and four pores.

As seen in Fig. 9, most of the features of AE events differ significantly between the two types of defects. The signal energy is the most significant feature, which means it has the most contribution to the defect classification (Fig. 9a). The features in the figure provide the greatest separation between the two defects.

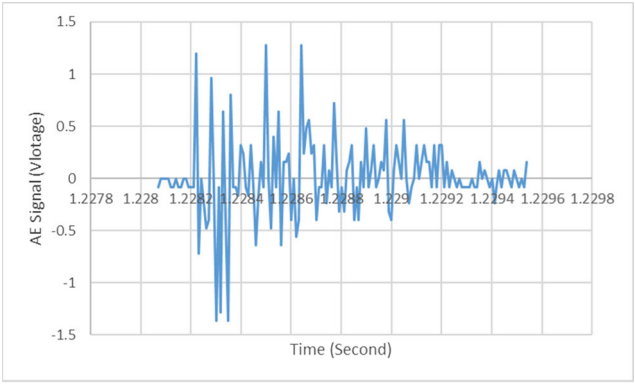

(a) Waveform signal sample emitted by a pore

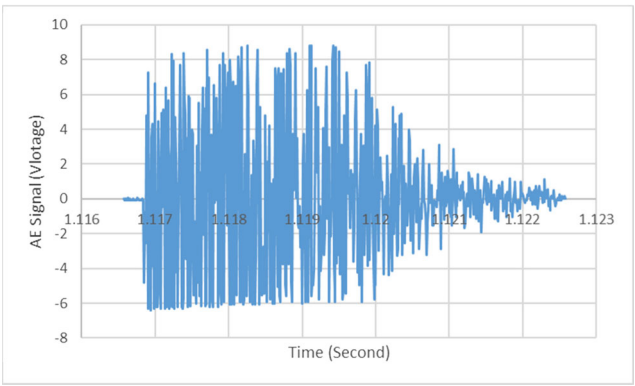

(b) Waveform signal sample emitted by a crack

Fig. 10 **a**, **b** Comparison between the waveforms emitted by cracks and porosities

Figure 10 shows waveform samples emitted by a pore and a crack, and it can be seen that the waveform created by a crack is quite different from the waveform from created by a pore. The cracks tend to create AE signals with high energy,

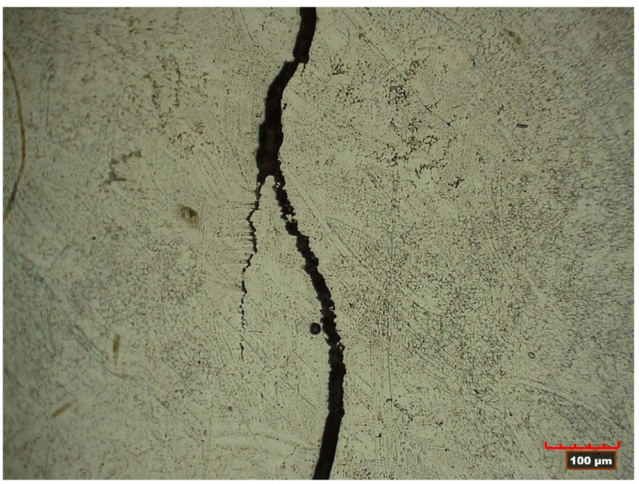

Fig. 11 Optical image of a transverse cross-sectioned laser deposit showing a crack

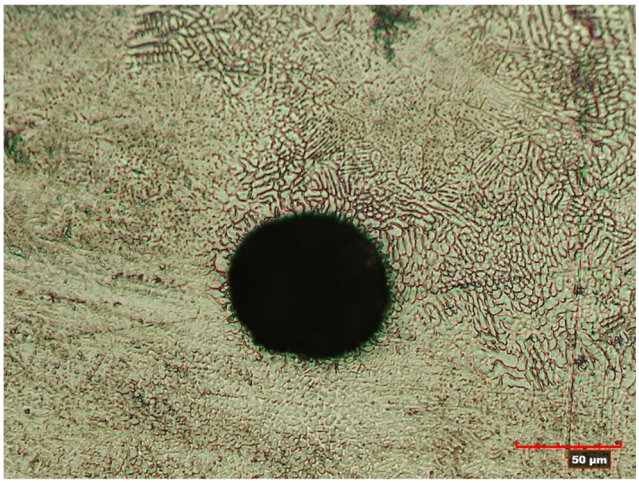

Fig. 12 Optical image of a transverse cross-sectioned laser deposit showing a gas porosity

longer duration, slower rise time, large number of counts, and higher amplitude when compared to the signals generated by porosities.

After preparing the surface of deposited metal, the cracks and pores were observed using an optical microscope. Figure 11 shows cracks caused by thermal stress. During laser deposition, the cracks are formed as result of thermal stress at the combining surface of deposition. The temperature gradient of the deposited layer is higher in the direction of thickness than other directions, and the thermal expansion coefficients are different for the two metal powders, which causes a thermal stress. It also occurs with powder contamination in the powder feeder [32].

The second type of observed defect is pores, which have a spherical form and appear in random locations that are not associated with the microstructure, as shown in Fig. 12. The possible sources of these porosities are surface powder contamination [32], gasses trapped within the powder particles due to the difference in the powder sizes, and an oxidation effect caused by the oxygen level being high due to not using the chamber to stimulate defect formation in this research. In fact, surface oxides may most likely remain in the solid state in the melting pool and, as such, upset the wetting mechanisms that melted the powder and induce voids.

4 Conclusions

In the presented paper, various types of LMD defects have been evaluated using AE technique. The results of this investigation showed that AE features were influenced by defect presence, and the findings exhibited the capability of AE technology to detect the presence of different defects in deposited material.

The AE signal was collected during the LMD in an oxidized environment with mixed metal powders in order to stimulate all possible types of defects. Several defect mechanisms were activated and detected by AE sensor. A LR model was implemented to analyze the AE signals and identify defect source mechanisms. The results were then compared to the outcomes of an ANN model, and both models demonstrated good agreement with the clustering analysis technique.

According to the logistic regression analysis, the frequency and kurtosis are not significant, which means that they have little contribution to the classification solution, their P values are greater than 0.05, three out of the seven detected defects are cracks, and the rest are pores. The mean squared error of the logistic regression and the neural network models are 1.72973 and 1.702703, respectively; there is an insignificant difference in the performance of the two models.

The LR and ANN successfully distinguished two primary defect types and their signal characteristics. Porosities produced AE signals with shorter decay time and less amplitude, while cracks triggered the AE signals with shorter durations and higher amplitudes; the signal energy is the most significant feature, which means it has the most contribution to the defect classification. AE offers the potential to detect and identify different LMD defects and thus assess the overall structural health of the part produced by LMD.

Acknowledgements This research was supported by the National Science Foundation grants IIP-1345240, CMMI-1301414, and CMMI-1547042. Support from the Product Innovation and Engineering, LLC, Missouri S&T Intelligent Systems Center, and the Missouri S&T Manufacturing Engineering Program is greatly appreciated.

References

1. Wang L, Felicelli SD, Craig JE (2009) Experimental and numerical study of the LENS rapid fabrication process. ASME J Manuf Sci Eng 131(4):041019-8. doi:10.1115/1.3173952
2. Weerasinghe VM, Steen WM (1983) Laser cladding by powder injection. In: Chen JMMM Chen, Tucker C (eds) Transport phenomena in materials processing, ASME, New York, pp 15–23
3. Weerasinghe V, Steen W (1987) Laser cladding with blown powder. Met Constr 19:581–585
4. Sears JW (1999) Direct laser powder deposition - 'State of the Art'. No. KAPL-P-000311; K99089 Knolls Atomic Power Lab, Nis, NY
5. McLean M (1997) Laser direct casting high nickel alloy components. Adv Powder Metall Part Mater 3:21
6. Mazumder J, Choi J, Nagarathnam J, Koch K, Hetzner D (1997) The direct metal deposition of H13 tool steel for 3D components. JOM 49:55–60
7. Lewis G, Nemec R, Milewski J, Thoma D (1994) Directed light fabrication, No. LAUR–94-2845; CONF-9410189–2, Los Alamos Natl. Lab., NM, USA
8. Milewski J, Lewis G, Thoma D (1998) Directed light fabrication of a solid metal hemisphere using 5-axis powder deposition. J Mater Process Technol 75:165–172

9. Wu X, Liang J, Mei J, Mitchell C, Goodwin PS, Voice W (2004) Microstructures of laser-deposited Ti-6Al-4V. Mater Des 25:137–144
10. Arcella F, Froes F (2000) Producing titanium aerospace components from powder using laser forming. JOM 52:28–30
11. Fessler JR, Merz R, Nickel AH, Prinz FB (1996) Laser deposition of metals for shape deposition manufacturing. In: Proceedings of the Solid Freeform Fabrication Symposium, University of Texas, Austin, pp 117–124
12. Keicher DM, Miller WD (1998) LENS moves beyond RP to direct fabrication. Met Powder Rep 53:26–28
13. Griffith M, Schlienger M, Harwell L (1998) Thermal behavior in the LENS process, No. SAND–98-1850C; CONF-980826. Sandia Natl. Labs, Albuquerque
14. Xue L, Islam M (1998) Free-form laser consolidation for producing functional metallic components. Laser Inst. Am. Laser Mater Process 84
15. Xue L, Islam M (2000) Free-form laser consolidation for producing metallurgically sound and functional components. J Laser Appl 12: 160–165
16. Ma Z, Sun G, Liu D, Xing X (2016) Dissipativity analysis for discrete-time fuzzy neural networks with leakage and time-varying delays. Neurocomputing 175(Part A):579–584
17. Gaja H, Liou F (2016) Automatic detection of depth of cut during end milling operation using acoustic emission sensor. Int J Adv Manuf Technol 86(9–12):2913–2925
18. Duro JA, Padget JA, Bowen CR, Alicia Kim H, Nassehi A (2016) Multi-sensor data fusion framework for CNC machining monitoring. Mech Syst Signal Process 66–67:505–520
19. Jolly, W. D. (1969) Acoustic emission exposes cracks during welding processes. Welding J 48
20. Rostek W (1990) Investigations on the connection between the welding process and airborne noise emission in gas shielded metal arc welding. Schw und Schn 42(6):E96–E97
21. Duley WW, Mao YL (1994) The effect of surface condition on acoustic emission during welding of aluminum with CO2 laser radiation. J Phys D Appl Phys 27:1379
22. Grad L, Kralj V (1996) On line monitoring of arc welding process using acoustic signals. In: Proceedings of the 13th Conference BIAM'96, Zagreb, pp i17–i20
23. Van Bohemen SMC, Hermans MJM, Den Ouden G (2001) Monitoring of martensite formation during welding by means of acoustic emission. J Phys D, Appl Phys (UK) (22):3312–3317
24. Grad L, Grum J, Polajnar I, Slabe JM (2004) Feasibility study of acoustic signals for on-line monitoring in short circuit gas metal arc welding. Int J Mach Tools Manuf 44(5):555–561
25. Yang Z, Yu Z, Wu H, Chang D (2014) Laser-induced thermal damage detection in metallic materials via acoustic emission and ensemble empirical mode decomposition. J Mater Process Technol 214(8):1617–1626
26. Diego-Vallejo D, Ashkenasi D, Eichler HJ (2013) Monitoring of focus position during laser processing based on plasma emission. Phys Procedia 41:911–918
27. Wang F, Mao H, Zhang D, Zhao X, Shen Y (2008) Online study of cracks during laser cladding process based on acoustic emission technique and finite element analysis. Appl Surf Sci 255 (5, Part 2): 3267–3275
28. Siracusano G, Lamonaca F, Tomasello R, Garesci F, La Corter A, Cani DL, Carpentieri M, Grimaldi D, Giovanni F (2016) A framework for the damage evaluation of acoustic emission signals through Hilbert–Huang transform. Mech Sys Signal Process 75: 109–122
29. Bianchi D, Vernes A (2015) Wavelet packet transform for detection of single events in acoustic emission signals. Mech Syst Signal Process 64–65:441–451
30. Gaja H, Liou F (2016) Defects monitoring of laser metal deposition using acoustic emission sensor. Int J Adv Manuf Technol:1–14
31. Cox DR (1958) The regression analysis of binary sequences. J R Stat Soc Ser B Methodol 20(2):251–242
32. Barua S et al (2014) Vision-based defect detection in laser metal deposition process. Rapid Prototyp J 20(1):77–85